ViTAE-SL: A vision transformer-based autoencoder and spatial interpolation learner for field reconstruction

Hongwei Fan, Sibo Cheng, Audrey J de Nazelle, Rossella Arcucci

ViTAE-SL: a vision transformer-based autoencoder and spatial interpolation learner for field reconstruction

Hongwei Fan[a,b], Sibo Cheng[d], Audrey J de Nazelle[b], Rossella Arcucci[c,a]

[a]*Data Science Institute, Imperial College London, London, UK*
[b]*Centre for Environmental Policy, Imperial College London, London, UK*
[c]*Department of Earth Science and Engineering, Imperial College London, London, UK*
[d]*CEREA, Ecole des Ponts and EDF R&D, Ile-de-France, France*

Abstract

Reliable and accurate reconstruction for large-scale and complex physical fields in real-time from limited observations has been a longstanding challenge. In recent years, sensors have been increasingly deployed in numerous physical systems. However, the locations of these sensors can shift over time, such as with mobile sensors, or when sensors are deployed and removed. These sparse and randomly located sensors further exacerbate the difficulty of reconstructing the physical field. In this paper, we present a new deep learning model called Vision Transformer-based Autoencoder (ViTAE) for reconstructing large-scale and complex fields. The proposed network structure is based on a novel core design: vision transformer encoder and Convolutional Neural Network (CNN) decoder. First, we split a two-dimensional field into patches and developed a vision transformer encoder to transfer patches into latent representations. We then reshape the linear latent representations to patches before concatenation, along with a CNN decoder, to reconstruct the field. The proposed model is tested in four different numerical experiments, using generated synthetic data, spatially distributed PM2.5 data, Computational Fluid Dynamics (CFD) simulation data and National Oceanic and Atmospheric Administration (NOAA) sea surface temperature data. The numerical results highlight the strength of ViTAE-SL compared to Kriging and state-of-the-art deep-learning models with significantly higher reconstruction

accuracy, computational efficiency, and robust scaling behavior.

Keywords: spatial interpolation, field reconstruction, vision transformer, autoencoder

1. Introduction

Advances in sensor technologies have enabled sensor deployments in physics system at a large scale. However, the number of monitoring sites within study areas is often relatively limited due to the high maintenance and setup costs. Sparsely scattered sensors are unable to capture whole physical fields in detail [1], and time-varying sensors further increase the difficulty of reconstructing the physical field; therefore robust and efficient spatial interpolation models are needed to reconstruct physical fields from limited and randomly localled sensor information. Spatial interpolation, which is predicting values of a spatial process in unmonitored areas from local sensor observations, is a major challenge in physics systems. Traditional applications of spatial interpolation include physics systems, environmental science, geophysics, astrophysics, atmospheric science, and fluid dynamics, and have been extended to other fields such as computer vision, public health, and biological sciences [2, 3, 4].

Kriging [5, 6] is a spatial interpolation method that offers linear unbiased prediction based on observations. Functioning as a Gaussian process [7] governed by covariance, Kriging extrapolates values in unobserved areas through a weighted average of observations. The computation of these weights necessitates the estimation of spatial covariance functions, conventionally assumed to be stationary within the framework of Kriging. However, real physical fields often have non-Gaussian and non-stationary spatial covariance functions [8, 9]. For example, the spatial covariance of PM2.5 concentrations usually changes a lot from one place to another, such as between cities and rural areas[10]. Therefore, Kriging may not always be optimal in practical real-world scenarios. In addition, kriging has limitations in handling large

spatial datasets due to its computational intensity. Finding the inversion of a $N \times N$ covariance matrix is needed to use Kriging. The number of observations, N, determines the size of the matrix, and the computation takes $O(N^3)$ time and $O(N^2)$ memory using the standard Cholesky decomposition method. Due to these limitations, it is challenging to utilize Kriging for real-time large-field reconstruction.

In recent years, deep learning (DL) [11] and neural network (NN) [12] have been extensively used in a wide spectrum of applications [13, 11]. DL has witnessed an explosion of architectures that are continuously evolving in both size and complexity, improving their capacity and capabilities in many different tasks [14, 15, 16, 17, 18, 19, 20, 21]. NNs are effective for predictions with complex features such as non-linearity and non-stationary. The use of GPUs has made NNs computationally efficient for analyzing large datasets.

Deep neural networks [11] have emerged as hopeful methods to reconstruct physical field from sparse measurements in an efficient manner [22, 23, 24, 19, 25]. Most neural networks require structure data, such as grid data. However, practical measurements are typically uneven or unstructured, such as air quality monitoring [26], hydrology measurement [27], and oceanographic observations [23]. Although graph neural network (GCN) [28] and multi-layer perception (MLP) [11] have the ability to process unstructured data, their scalability is limited due to the high computational cost. Furthermore, these methods require fixed numbers and positions of measurements as input data and cannot accommodate time-varying sensors, rendering them impractical in real-world physical field reconstruction, where the numbers and positions of sensors typically change over time [29].

To address these two bottlenecks, Fukami et al. [30] employed Voronoi tessellation to convert observations into a structured grid format that is compatible with convolutional neural network (CNN) and then utilized CNN to reconstruct the field from the structured grid. However, convolutions typically operate on a small patch of field to extract features but do not encode

the relative position of different features. This makes it difficult for CNN to explore spatial dependencies for large field reconstruction [31], especially when the observations are very sparse. For example, air pollution monitoring sites are often sparsely distributed in large areas, making the reconstruction of air pollution maps on a fine scale a longstanding challenge [32].

The introduction of Vision Transformers (ViT) [33]has the potential to address this challenge. Transformers, originally proposed by Vaswani et al.(2017) [14], have emerged as a prominent technique in the field of Natural Language Processing (NLP) due to their ability to capture long-range dependencies and learn contextual relationships effectively. Besides the advanced structure of transformers, the training strategy is also crucial for the success of this NLP models: They involve removing a portion of the text and learning to predict the removed content. This strategy, known as auto-encoding, is applied in various fields, such as computer vision and flow problems, and demonstrates encouraging outcomes [34, 35]. For example, He et al. [36] showed that by employing masked autoencoders (AEs) to remove random sections of the input image and then rebuild those missing sections, it is possible to rebuild images that appear realistic, even when more than 90% of the image is masked. Rebuilding images from random visible patches is conceptually similar to field reconstruction from observations.

While the ViT model and the autoencoder (AE) method [36] have achieved success in image reconstruction, as far as we know, there is no prior research on field reconstruction by ViT. There are two problems that hinder the application of these methods in the field reconstruction task:

- ViT typically predicts masked image patches using visible patches. Compared to image patches with values on each pixel, the observations in this study are sparse in each patch. Setting the patch size of 1×1 pixel in ViT will lead to high computational cost, which makes the model applicable only to small resolution fields.

- ViT predicts each patch separately. Concatenating the predicted patches

can result in heterogeneous and inconsistent reconstructions [36].

This paper proposes using ViT and AE for large physical field reconstruction from sparse and time-varying observations.

2. Contribution of the present work

Inspired by the success of ViT and AE methods, we introduce a new deep learning model called Vision Transformer-based autoencoder and spatial interpolation learner (ViTAE-SL) for reconstructing large-scale and complex fields. More precisely, the proposed framework consists of a ViT as the encoder and a CNN as the decoder. In order to tackle the challenges mentioned earlier, we propose a method that involves incorporating sparse sensor data into a Transformer. This is achieved by mapping the observations in the grid field and masking the unmonitored grids. The next step involves splitting the observations field into patches and feeding them into the transformer encoder to obtain features. These features are then reshaped into patches and concatenated together. To bridge the gap between patches and make the reconstruction field more consistent, we use the CNN decoder to predict grid values based on concatenated patches. Following this structure, our ViTAE-SL is capable of fast and accurate field construction using time-varying and unstructured observations. Four test cases, including synthetic data and real-world applications, are implemented in this study to compare the performance of the proposed ViTAE-SL against state-of-the-art field reconstruction methods.

The subsequent sections of the paper are structured in the following manner: Section 3 introduces the construction and properties of ViTAE-SL model. Section 4 showcases four case studies that demonstrate the efficacy of ViTAE-SL. Section 5 summarizes our primary findings and proposes potential areas for future research.

3. Methodology

Our objective is to reconstruct a two-dimensional global field variable $\boldsymbol{Q} \in \mathbb{R}^{n_x \times n_y}$ from a vector of local sensor measurements $\boldsymbol{s} \in \mathbb{R}^n$, locations $x_{si} \in \mathbb{R}^2, i = 1, \ldots, n$. Here, n_x and n_y respectively denote the number of grid points in the horizontal and vertical directions on a high-resolution field, and n indicates the number of local sensor measurements. ViTAE-SL is an autoencoding approach that reconstructs the original field-given observations. To handle the sparse observations and learn efficient representations from them, we adopt a ViT-based encoder that allows us to operate on the observations. After that, a lightweight CNN decoder is used to reconstruct the full grid field from the latent representations. Figure 1 illustrates the flowchart of the proposed approach. In what follows, we introduce the ViT-based encoder and CNN decoder, which are the two key components in the present approach.

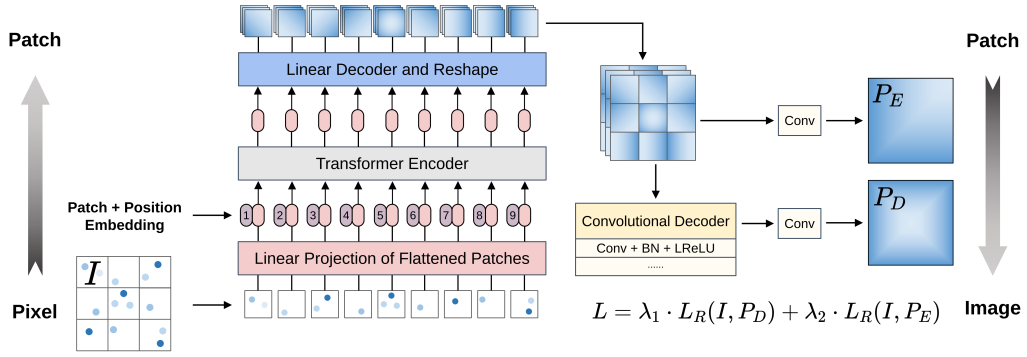

Figure 1: Model overview of ViTAE-SL. We split the grid field into fixed-size patches, linearly embed each of them, add position embeddings, and feed the resulting sequence of vectors to a standard Transformer encoder. After that, we used a CNN decoder to predict the grid values from the encoder's latent.

ViT-based encoder. First, we transform observations into grid fields based on their location to allow use of ViT, defined as:

$$I\left(\{\boldsymbol{x}_{\boldsymbol{s}i}\}_{i=1}^{n}\right) = \begin{cases} x_i & \text{for any location } \boldsymbol{x}_{\boldsymbol{s}i} \\ 0 & \text{otherwise.} \end{cases} \tag{1}$$

n is the number of observations, where x_i denotes the value of the i-th observation. We start by spliting the grid field $I \in \mathbb{R}^{n_x \times n_y}$ into patches $\mathbf{x}_p \in \mathbb{R}^{N \times (P_h \times P_w)}$, where $P_h \times P_w$ is the resolution of each patch. N is the corresponding number of split patches and is also the input sequence length of ViT. Using a patch embedding projection $\mathbf{E}$, the patches are mapped to the embedding of dimensions $D = P_h \times P_w$. Then, positional embeddings $\mathbf{E}_{pos}$ are added and fed into a series of Transformer blocks to obtain latent representations.

The processing of encoder can mathematically be formulated as:

$$\begin{aligned} \mathbf{z}_0 &= \left[{\mathbf{x}_p}^1\mathbf{E}; {\mathbf{x}_p}^2\mathbf{E}; \cdots; {\mathbf{x}_p}^N\mathbf{E}\right] + \mathbf{E}_{pos}, && \mathbf{E} \in \mathbb{R}^{(P_h \cdot P_w) \times D}, \mathbf{E}_{pos} \in \mathbb{R}^{N \times D} \\ \mathbf{z}'_\ell &= \mathrm{MSA}\left(\mathrm{LN}\left(\mathbf{z}_{\ell-1}\right)\right) + \mathbf{z}_{\ell-1}, && \ell = 1 \ldots L \\ \mathbf{z}_\ell &= \mathrm{MLP}\left(\mathrm{LN}\left(\mathbf{z}'_\ell\right)\right) + \mathbf{z}'_\ell, && \ell = 1 \ldots L \\ \mathbf{y} &= \mathrm{LN}\left(\mathbf{z}_L^0\right) \end{aligned} \tag{2}$$

The Transformer encoder consists of L layers of multiheaded self-attention (MSA) and multilayer perceptron (MLP) blocks. Layernorm (LN) is applied before every block, and residual connections are applied after every block. y is the output of the encoder. The length of y is equal to the number of grids in a patch. We reshape the vectors into patches and concatenate these patches to form a field-shaped representation, which is used as the input to a CNN-based decoder. Additionally, a convolution layer is applied to produce $P_E \in \mathbb{R}^{n_x \times n_y}$ based on the field-shaped representation.

CNN-based decoder. The CNN-based decoder consists of sequences of convolutional layers, batch normalization, and activation layers. Batch normalization is applied after each convolutional layer to normalize the output before passing it through the activation layers. The parameters of the CNN-based decoder are shown in 3. The CNN-based decoder receives the field-shaped representation produced by the encoder as input, and the output of the decoder is the predicted field $P_D \in \mathbb{R}^{n_x \times n_y}$ that corresponds to the entire field $\boldsymbol{Q}$.

$$\begin{aligned} P'_\ell &= \text{Conv2D}\left(P_{\ell-1}, \boldsymbol{W}_\ell\right), \quad \ell = 1 \dots L \\ P_\ell &= \text{ReLU}(P'_\ell), \quad \ell = 1 \dots L \end{aligned} \tag{3}$$

where $\boldsymbol{W}$ denotes weights (filters) of CNN. The output of each filter operation is passed through an activation function which is chosen to be the rectified linear unit (ReLU).

Reconstruction target. Our ViTAE-SL reconstructs the field by predicting the values for each grid. The loss function computes the mean squared error (MSE) between the reconstructed P_E, P_D and original fields $\boldsymbol{Q}$ in pixel space. L_R denotes the mean squared error. The loss is defined as:

$$L = \lambda_1 \cdot L_R\left(Q, P_D\right) + \lambda_2 \cdot L_R\left(Q, P_E\right) \tag{4}$$

Where λ_1 and λ_2 are the weights for balancing the multiple objectives.

4. Test cases and results

In this section we thoroughly demonstrate the performance of present ViTAE-SL for field reconstruction with extensive numerical experiments under different circumstances. Our examples include:

- Simulation data produced by Gaussian covariance models
- China air quality dataset

- Fluid dynamics data of unsteady wake flow
- NOAA global sea surface temperature

These datasets have different characteristics in terms of structured or unstructured field, time varying data and observation noise as shown in Table 1. The performance of the field reconstruction methods: ViTAE-SL, Kriging and Voronoi tessellation-assisted convolutional neural network (VCNN) have been evaluated on both structured and unstructured data. For example, the unsteady wake flow is based on two-dimensional irregular meshes. However, all observations used in this study are unstructured. The first test case consists of simulation data generated by Gaussian covariance model and the observable points are randomly selected and time-varying. Spatially distributed air quality observations come from the Chinese regulatory monitor stations [37] which change over time. Unsteady wake flow has fixed but very sparse observations. As for the National Oceanic and Atmospheric Administration (NOAA) sea surface temperature data, we select different numbers of observations as the train and test dataset, which are time-varying. These datasets are chosen to evaluate the performance of ViTAE-SL for handling sparse, unstructured and time-varying data.

Table 1: Different test cases performed in this paper

Test case	unstructured field	unstructured observation	time-varying sensors	observation noise
simulation data	✗	✓	✓	✗
Air quality	✓	✓	✓	✓
Unsteady wake flow	✓	✓	✗	✗
NOAA	✓	✓	✓	✗

4.1. Test case 1: Simulation data

In this section, we evaluate the performance of ViTAE-SL against Kriging and VCNN in stationary simulation data.

In order to replicate a physically uniform field, the simulation field data are created using the gstool [38], with a Gaussian covariance kernel with a correlation scale length of $L \in (40, 80)$. This means that the correlation between two points in the field only depends on their spatial distance, which is ideal for the Kriging method. These simulations are commonly used to compare different field reconstruction methods [39].

After creating the grid field, grid points are randomly selected as observations. Unlike VCNN and ViTAE-SL, the Kriging method requires prior knowledge of the covariance kernel. Numerical experiments on Kriging are conducted using two kernel functions: Gaussian and Exponential, both with the exact correlation length used for data generation. The latter is used to simulate situations where the kernel function is misjudged, as in real-world scenarios, the exact covariance kernel is often difficult to determine [40].

Figure 2 illustrates the computational time of Kriging (using the Gaussian kernel) for reconstructing various field sizes based on different numbers of observations. It's observed that as the field size and the number of observations increase, the computational time for Kriging grows exponentially. This poses computational challenges for large-scale field reconstruction with Kriging. For instance, when the field size exceeds 256 and the number of observations is more than 0.1%, Kriging requires thousands of seconds to fit and predict.

In order to compare the performance of ViTAE-SL against VCNN and Kriging, we conducted experiments on a field size of 512 x 512. The number of observations used for training was set to 0.5%, 1%, 2%, and 5% of the total number of grid points in the field. For each observation ratio, we generated 10,000 field snapshots and randomly selected observations from each snapshot, resulting in time-varying observation placement. We used an

80/10/10 split for training, validation, and testing datasets.

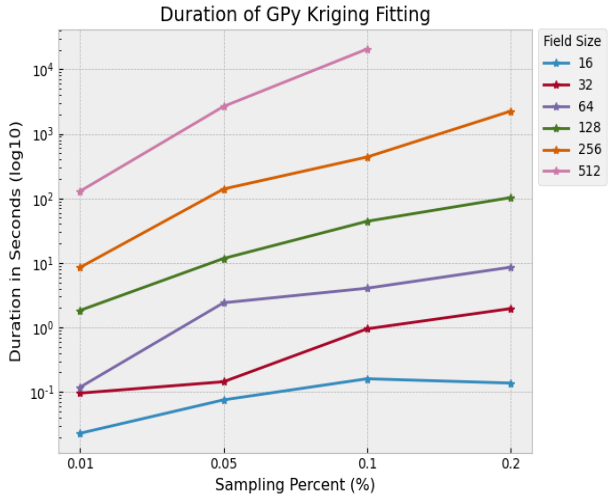

Figure 2: Execution time of Kriging for different size of the field.

We use the original ViT setup [33] for the ViT-based encoder design and employ "Lite", "Base", and "Large" models as summarized in Table 2. In the following sections, we'll use abbreviated notation to denote the model size and the input patch size. For instance, ViTAE-large/16 represents combination of the "Large" version of ViT in Table 2 and CNN in Table 3 with 16×16 input patch size.

Model	Layers	Hidden Size D	Heads	Channel	Patch Size
ViT-Lite	8	32	8	16	16
ViT-Base	8	64	8	32	16
ViT-Large	8	128	8	64	16

Table 2: Details of Vision Transformer encoder variants.

For the CNN-based decoder, we use a sample convolutional neural network; the configurations of each decoder for "Lite", "Base", and "Large" models are shown in Table 3. The CNN-based decoder is trained to estimate

the whole simulation field based on intermediate features from ViT-based encoder.

Model	Layers	Channel D	filter size
CNN-Lite	5	16	3
CNN-Base	5	32	3
CNN-Large	5	64	3

Table 3: Details of CNN decoder variants.

As shown in Figure 3, the field reconstruction from the ViTAE-SL closely resembles the ground truth (GT) without prior knowledge.

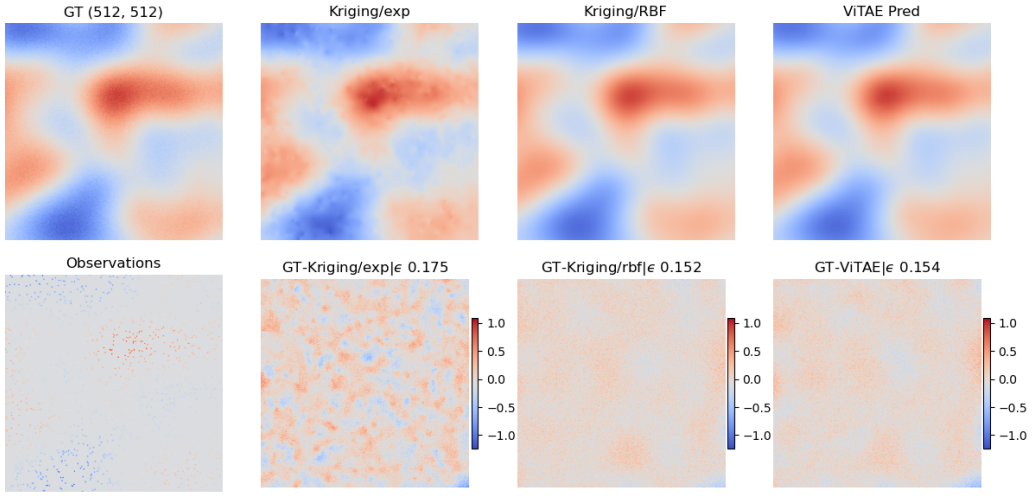

Figure 3: 512×512 Gaussian field reconstruction results of ViTAE-SL and Kriging , 0.5% sampling rate compare to the GT.

Figure 3 also reports the relative error defined as:

$$\epsilon = \frac{\|Q_{\text{ref}} - Q_{\text{reconstruct}}\|_2}{\|Q_{\text{ref}}\|_2}, \tag{5}$$

where $\|\cdot\|$ denotes the L_2 norm, and Q_{ref} and $Q_{\text{reconstruct}}$ are the reference and reconstructed fields, respectively. The relative error metric is commonly

used in field reconstruction and prediction tasks [41, 42]. In our study, we compared Kriging's reconstruction results with Gaussian and exponential covariance kernels, referred to as Kriging/RBF and Kriging/exp, respectively. Figure 3 clearly shows that the Kriging/RBF model greatly outperforms the Kriging/exp model, suggesting that Kriging is vulnerable when the covariance kernel is not accurately specified. However, ViTAE-SL created reconstruction results that were nearly as precise as those of Kriging/RBF without any prior information. Besides, ViTAE-SL is much more efficient than Kriging, as shown in Table 5. For example, ViTAE-SL-lite/16 runs 10^6 faster than Kriging when the field size is 512 and the ratio of observation grids is 5%.

Model	ϵ			
Kriging/RBF	0.2243	0.2221	0.2218	0.2215
Kriging/Exp	0.2553	0.2552	0.2550	0.2379
VCNN	0.2324	0.2259	0.2216	**0.2160**
ViTAE-lite/16	0.2431	0.2346	0.2290	0.2242
ViTAE-base/16	0.2280	0.2369	0.2250	0.2234
ViTAE-large/16	**0.2255**	**0.2228**	**0.2213**	0.2202
Sampling Percent	0.5%	1%	2%	5%

Table 4: Gaussian field reconstruction result of ViTAE-SL, VCNN and Kriging.

Model	Execution time (s)			
Kriging/RBF	21	59	191	1491
Kriging/Exp	31	76	253	1586
VCNN	0.035	0.035	0.035	0.035
ViTAE-lite/16	0.0105	0.0104	0.0105	0.0106
ViTAE-base/16	0.0128	0.0127	0.0128	0.0128
ViTAE-large/16	0.0150	0.0154	0.0151	0.0153
Sampling Percent	0.5%	1%	2%	5%

Table 5: Execution time in seconds of the Gaussian field reconstruction for ViTAE-SL, VCNN and Kriging.

We also compare ViTAE-SL with the VCNN [30]. Table 4 shows the online computational time and the ϵ values for ViTAE-SL, VCNN and Krig-

ing for different numbers of observations in 512×512 field reconstruction. These results show that ViTAE-SL outperforms VCNN when observations are sparse (less than 2% in this case), demonstrating the strength of ViTAE-SL in handling sparse observations.

4.2. Test case 2: Chinese air quality

To evaluate the performance of ViTAE-SL in real-world physical field reconstruction problems, we first applied our approach to the PM2.5 concentration dataset in China. The ChinaHighPMC [37] dataset consists of daily air pollutants at ground level PM2.5 for China with 1km resolution. These data are extracted and combined from different resources, including ground-based measurements, satellite remote sensing products, atmospheric reanalysis, and model simulations. In particular, we utilise the 5km, 10km and 20km resolution grid fields for the Chinese area, so the corresponding shapes of the entire field are 714×1229, 357×615 and 184×312. Unstructured observations from monitor stations [43] are projected in the grid field. Since sensors are affected by ambient factors, noise is included in these observation values. When there are several monitor stations in one grid cell, the value is calculated as the average observation values. The daily air quality field and corresponding observations span from 2013 to 2020 and the total number of snapshots is 2992. We randomly selected 80% of the snapshots as training data sets, 10% are used as validation dataset and 10 % for testing dataset. The average number of observations is 1173, resulting in 0.13%, 0.52% and 2.08% against the total number of grid points in 5km, 10km and 20km resolution grid fields.Table 6 shows the model parameters of the ViT-based encoder and Table 7 shows the corresponding parameters of the CNN-based decoder.

ViTAE-SL is compared with the Kriging method and the VCNN. Kriging has been previously applied in a similar circumstance [44]. The performance of ViTAE-SL spatial data recovery for air pollution in China is shown in Figure 4. The reconstructed field by ViTAE-SL shows great agreement with the reference data in the test dataset. The advantage of ViTAE-SL is in partic-

Model	Layers	Hidden Size D	Heads	Channel	Patch Size
ViT-Lite/32	8	32	8	16	32
ViT-Base/32	8	64	8	32	32
ViT-Large/32	8	128	8	64	32

Table 6: Vision Transformer encoder Parameters used in the study case of Chinese air quality.

Model	Layers	Channel D	filter size
CNN-Lite	5	16	3
CNN-Base	5	32	3
CNN-Large	5	64	3

Table 7: CNN decoder parameters used in the study case of Chinese air quality data.

ular significant when comparing the contours of reconstruction. Table 8 and Table 9 show the online computational time and metrics of ViTAE-SL, VCNN and Kriging in the China air quality field reconstruction task, which demonstrate that ViTAE-SL spends much less time than kriging with a much better performance. Moreover, in terms of reconstruction accuracy, ViTAE-SL outperforms VCNN when the observations are sparse (i.e., 0.13% and 0.52%). In fact, by construction, ViTAE-SL is powerful in capturing chaotic local patterns in real-world field reconstruction task. To further evaluate the reconstruction performance, two image similarity metrics Peak Signal-to-Noise Ratio (PSNR) and Structural Similarity Index Measure (SSIM) [45] are employed to compare the reconstructed field against the original one. These metrics are widely used for similarity measures robust to rotation and translation [46]. As shown in Figure 4, ViTAE-SL also has a higher PSNR and SSIM scores compared to Kriging and VCNN. These results speak to the significant advantage of ViTAE-SL in a real-world field reconstruction problem.

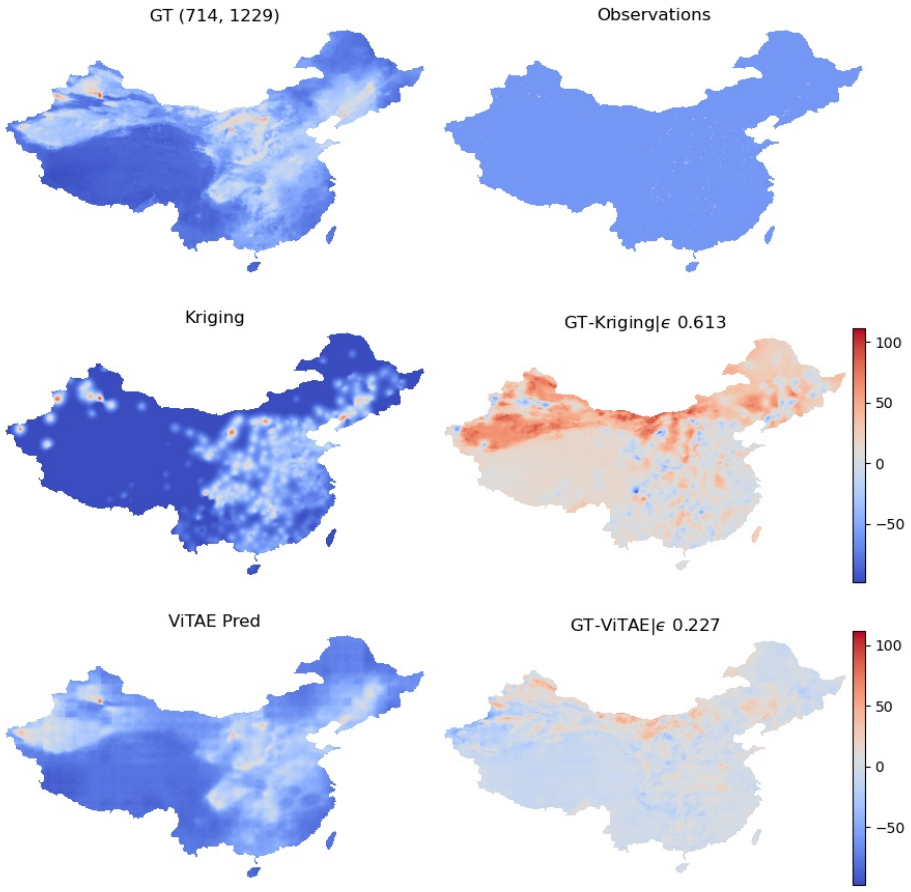

Figure 4: China air quality reconstruction results of ViTAE-SL and Kriging and comparison to the GT.

4.3. Test case 3: unsteady wake flow

To compare ViTAE-SL with the state-of-the-art VCNN in the case of unstructured grids and extremely sparse observations, we consider the two-dimensional unsteady laminar cylinder wake data. This test case was used in [30] for demonstrating the capability of VCNN . The training data set is prepared with a direct numerical simulation, which numerically solves the incompressible Navier–Stokes equations. In this study, we aim to reconstruct the vorticity field and we consider the same data that were used in [30]. The

Model	ϵ			Execution time (s)
Kriging	0.8599	0.8195	0.5520	117.5
VCNN	0.3978	0.3527	0.3261	0.0063
ViTAE-lite	0.3571	0.3389	0.3245	0.0053
ViTAE-base	0.3570	0.3434	0.3129	0.0058
ViTAE-large	**0.3566**	**0.3371**	**0.3205**	0.0061
Monitor Percent	0.13%	0.52%	2.08%	0.13%

Table 8: Performance in terms of Loss and execution time of ViTAE-SL, VCNN and Kriging for different observation density of China air quality reconstruction.

Model	SSIM			PSNR		
Kriging	0.7788	0.8195	0.8517	24.0098	25.0369	25.8168
VCNN	0.9385	0.9340	0.9321	29.7478	30.3167	30.4041
ViTAE-lite	0.9421	0.9330	0.9271	30.8184	30.8221	30.4489
ViTAE-base	0.9451	0.9366	0.9377	30.9079	30.7691	30.8588
ViTAE-large	**0.9471**	**0.9399**	**0.9304**	**30.9466**	**30.9628**	**30.6220**
Monitor Percent	0.13%	0.52%	2.08%	0.13%	0.52%	2.08%

Table 9: Performances of ViTAE-SL, VCNN and Kriging for different observation density of China air quality reconstruction.

shape of the entire field is 192×112. The data span approximately 4 vortex shedding periods and the total number of snapshots is 5000. We randomly selected 80% of the snapshots as training data sets, 10% are used as validation dataset and 10% for testing dataset. The number of sensors is set to 8 with fixed input sensor locations for both training and testing. Here we use the same model parameters as in Section 4.2. Figure 5 illustrates an example of the reconstruction fields in the testing dataset using VCNN and ViTAE-SL with the position of sensors. As shown in Figure 5, the vorticity fields reconstructed by ViTAE-SL are close to the GT. It can be seen from the reconstructed vorticity field that VCNN shows considerable reconstruction error due to the small number of sensors; however, ViTAE-SL provides significantly more accurate reconstruction over the whole field in this example. Table 10 illustrates the averaged value of three different metrics, namely ϵ, PSNR and SSIM, over the testing dataset. Consistent with our analysis

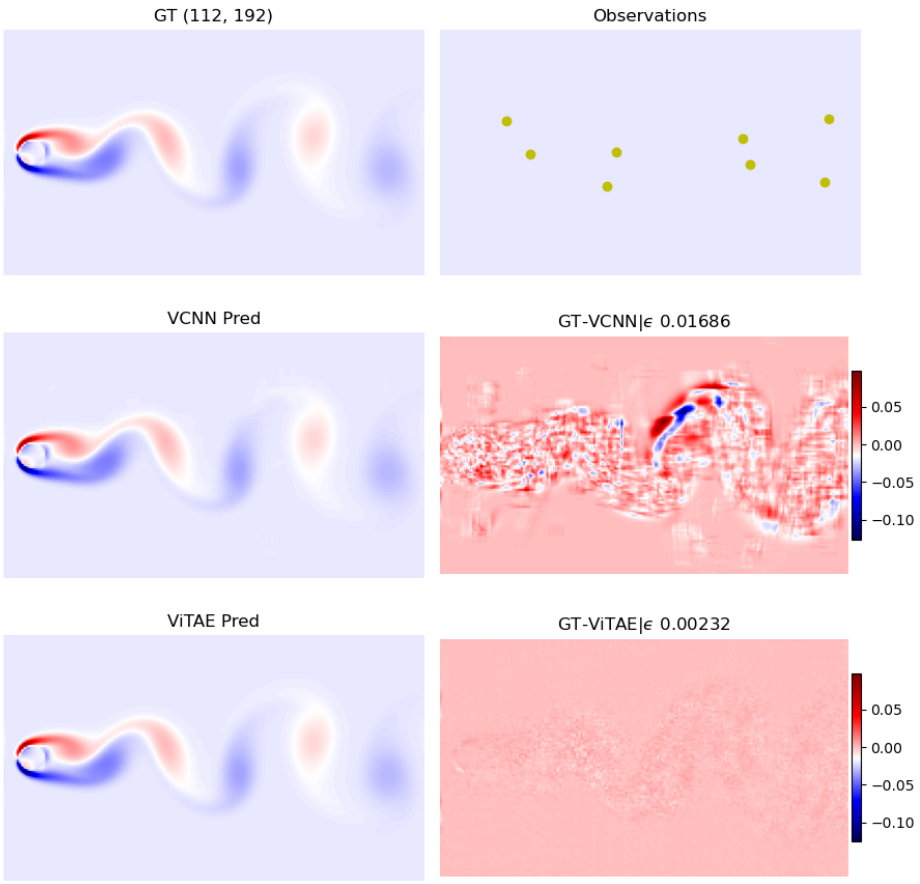

Figure 5: Unsteady wake flow reconstruction results of ViTAE-SL and VCNN compared to the GT.

of Figure 5, ViTAE-SL also outperforms VCNN in all three metrics. Both ViTAE-SL and VCNN run less than $0.01s$ in this reconstruction task. We here did not compare our results against Kriging, due to its poor performance with such sparse observations. This study shows that interpolation schemes, such as Kriging, and CNN-based methods, such as VCNN, are unable to reconstruct the fine-grained features of fields accurately if the observations are extremely sparse (e.g., 0.06% in this study). However, the proposed ViTAE-SL model is able to deliver a fast and accurate reconstruction of the

vorticity field of dimension using only 8 sensors.

Model	ϵ	PSNR	SSIM	Execution time (s)
VCNN	0.0230	64.55	0.9988	0.0016
ViTAT-lite/8	0.0112	70.63	0.9988	0.0043
ViTAE-base/8	0.0050	77.56	0.9999	0.0050
ViTAE-large/8	**0.0023**	**84.37**	**0.9988**	0.0052

Table 10: Unsteady wake flow reconstruction performances of ViTAE-SL and VCNN.

4.4. Test Case 4: NOAA global sea surface temperature

To show the capacity of ViTAE-SL in global physical field reconstruction, we used NOAA sea surface temperature data collected from satellite and ship-based observations. Data are made up of weekly observations of sea surface temperature with a spatial resolution of 360 $\times$ 180. To make a fair comparison against VCNN [30], we use the same data set in [30]. 1040 snapshots span from 1981 to 2001 are used to train the models and the test snapshots are taken from 2001 to 2018. In this test case, sensors are supposed to be randomly placed over the field. The number of sensors for training is set to $n_{\text{sensor,train}} = 10, 20, 30, 50, 100$ and for the test data, we also consider unseen cases with 70 and 200 sensors such that $n_{\text{sensor,test}} = 10, 20, 30, 50, 70, 100, 200$.

An example of global sea surface temperature reconstruction using 10 sensors in the testing dataset is displayed in Figure 6. A significant advantage of the proposed ViTAE-SL model can be clearly observed with a considerably lower reconstruction error. The values of ϵ as defined in (5) are also indicated in Figure 6. As shown in Figure 6, the VCNN model fails to accurately reconstruct the details of the temperature fields when the number of sensors is severely limited (10 trained sensors in this case). In fact, the field reconstructed by VCNN also exhibits some non-realistic discontinuities due to the small number of sensors. On the other hand, the proposed ViTAE-SL is

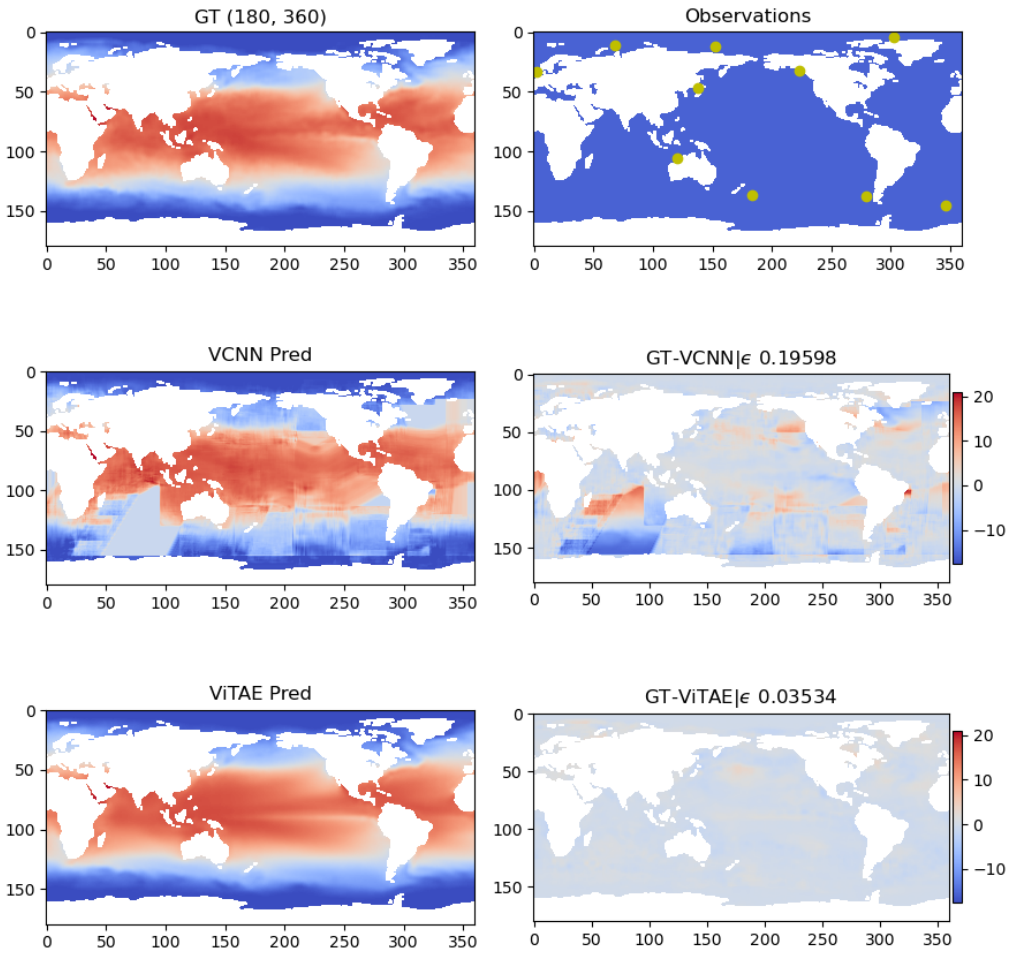

Figure 6: NOAA field reconstruction performance of ViTAE-SL and VCNN for trained 10 input observations, compared to the GT.

capable of delivering smooth and accurate reconstruction of the temperature field.

In this test case, we also aim to evaluate the impact of the number of sensors on the performance of VCNN and ViTAE-SL in terms of reconstruction accuracy. We plot the evolution of the ϵ error of both training and testing data against the number of sensors in Figure 7. As shown by the dashed

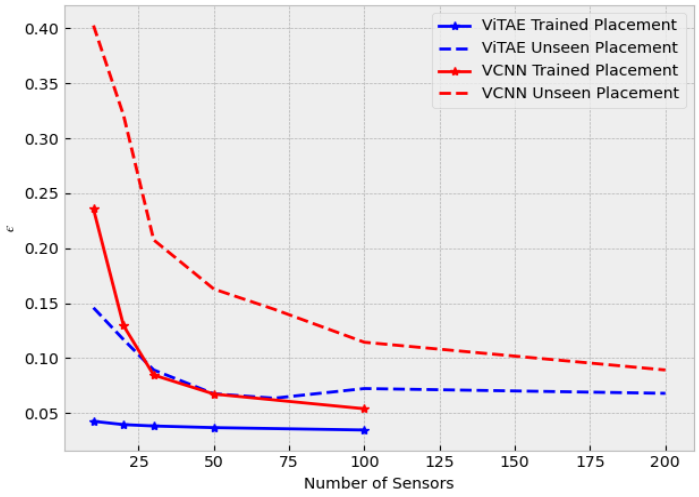

Figure 7: NOAA field reconstruction performances of ViTAE-SL and VCNN for various input observations.

blue line, when the number of sensors is over 30 for the test data, ViTAE-SL achieves a reasonably good reconstruction with the ϵ error being less than 0.1. However, as shown by the dashed red line, VCNN requires more than 200 sensors to obtain the same accuracy. In fact, the training of ViTAE-SL (solid blue line) also converges much faster compared to VCNN (solid red line).

5. Conclusion and Future Works

Spatial interpolation from sensor observations has been a longstanding challenge in physics systems. In order to address this problem, the paper proposes a novel ViT-based autoencoder which is an efficient spatial interpolation learner. The proposed novel method ViTAE-SL relies an attention mechanism in ViT to specify the sensor location and the global spatial dependence of the sensor measurements. The use of ViT splits the input sensor data to patches and translates patches into latent variables by a transformer block, which relying entirely on an attention mechanism to draw global de-

pendencies. Then the use of CNN decoder converts the latent variables to patches before concatenation. This process then enables the applications of CNNs to derive grid field reconstruction. The Vision Transformer encoder allows more parallelization and this requires significantly less computational time, which is crucial for large physical field reconstruction tasks. The CNN decoder also contributes to the physical field reconstruction consistency. The proposed method combines the advantages of both ViT and CNN, which make it outperform Kriging and the state-of-the-art VCNN.

The numerical results presented in the four test cases in this paper clearly suggests that the novel ViTAE-SL significantly outperforms the interpolation-based Kriging method and the CNN-based VCNN method. In particular, compared to Kriging, ViTAE requires no prior knowledge of the spatial distribution and reduces considerably the computational cost. The advantage of ViTAE-SL compared to VCNN is more significant when the data are sparse and unstructured, showing a great capacity of capturing spacial dependancy. In summary, these experiments demonstrate that ViTAE-SL is capable of dealing with nonstationarity, nonlinear relationships, and non-Gaussian field reconstruction from scattered observations.

This work has provided a new perspective on DL in spatial prediction and could be applied to a wide range of studies of complex physics systems. In the future, the proposed method could be extended to a multivariate system to explore relationships and correlations between heterogeneous data. For example, this proposed method could be applied to integrate various types of measurements, such as low-cost air quality sensors, emission invention, traffic flow, and meteorological measurements, to enhance air quality field predictions. In this sense, it goes beyond spatial interpolation methods. This perspective allows researchers to explore the wealth of sensors measurements using data-driven technique, and will support scientific endeavor across a wide range of studies in physics system, spatio-temporal statistics and geostatistics.

Code and data availability

The code has been implemented using python and available at `https://github.com/fanhongweifd/ViTAE-for-field-reconstruction`. All experiments are finished with the same RTX 3080 GPU.

Acknowledgement

This work is supported by the EPSRC grant EP/T003189/1 Health assessment across biological length scales for personal pollution exposure and its mitigation (INHALE). Sibo Cheng acknowledges the support of the French Agence Nationale de la Recherche (ANR) under reference ANR-22-CPJ2-0143-01.

Acronyms

DL	deep learning
NN	neural network
AE	autoencoder
NLP	Natural Language Processing
CNN	convolutional neural network
VCNN	Voronoi tessellation-assisted convolutional neural network
SSIM	Structural Similarity Index Measure
PSNR	Peak Signal-to-Noise Ratio
ViT	Vision Transformers
ViTAE-SL	Vision Transformer-based autoencoder and spatial interpolation learner
MLP	multi-layer perception
GCN	graph neural network

GT ground truth

MSE mean squared error

References

[1] Y. Cheng, X. Li, Z. Li, S. Jiang, Y. Li, J. Jia, X. Jiang, Aircloud: A cloud-based air-quality monitoring system for everyone, in: Proceedings of the 12th ACM Conference on Embedded Network Sensor Systems, 2014, pp. 251–265.

[2] N. Cressie, Statistics for spatial data, John Wiley & Sons, 2015.

[3] M. P. Austin, Spatial prediction of species distribution: an interface between ecological theory and statistical modelling, Ecological modelling 157 (2-3) (2002) 101–118.

[4] L. A. Waller, C. A. Gotway, Applied spatial statistics for public health data, John Wiley & Sons, 2004.

[5] M. A. Oliver, R. Webster, Kriging: a method of interpolation for geographical information systems, Int. J. Geogr. Inf. Sci. 4 (1990) 313–332.

[6] N. Cressie, The origins of kriging, Mathematical Geology 22 (1990) 239–252.

[7] C. E. Rasmussen, Gaussian processes in machine learning, in: Summer school on machine learning, Springer, 2003, pp. 63–71.

[8] C. J. Paciorek, M. J. Schervish, Spatial modelling using a new class of nonstationary covariance functions, Environmetrics: The official journal of the International Environmetrics Society 17 (5) (2006) 483–506.

[9] H. Zareifard, M. J. Khaledi, Non-gaussian modeling of spatial data using scale mixing of a unified skew gaussian process, Journal of Multivariate Analysis 114 (2013) 16–28.

[10] F. Karagulian, C. A. Belis, C. F. C. Dora, A. M. Prüss-Ustün, S. Bonjour, H. Adair-Rohani, M. Amann, Contributions to cities' ambient particulate matter (pm): A systematic review of local source contributions at global level, Atmospheric environment 120 (2015) 475–483.

[11] Y. LeCun, Y. Bengio, G. Hinton, Deep learning, nature 521 (7553) (2015) 436–444.

[12] A. Krizhevsky, I. Sutskever, G. E. Hinton, Imagenet classification with deep convolutional neural networks, Communications of the ACM 60 (6) (2017) 84–90.

[13] G. Hadash, E. Kermany, B. Carmeli, O. Lavi, G. Kour, A. Jacovi, Estimate and replace: A novel approach to integrating deep neural networks with existing applications, arXiv preprint arXiv:1804.09028 (2018).

[14] A. Vaswani, N. Shazeer, N. Parmar, J. Uszkoreit, L. Jones, A. N. Gomez, Ł. Kaiser, I. Polosukhin, Attention is all you need, Advances in neural information processing systems 30 (2017).

[15] K. He, X. Zhang, S. Ren, J. Sun, Deep residual learning for image recognition, in: Proceedings of the IEEE conference on computer vision and pattern recognition, 2016, pp. 770–778.

[16] C. Q. Casas, R. Arcucci, P. Wu, C. Pain, Y.-K. Guo, A reduced order deep data assimilation model, Physica D: Nonlinear Phenomena 412 (2020) 132615.

[17] S. Cheng, C. Quilodrán-Casas, S. Ouala, A. Farchi, C. Liu, P. Tandeo, R. Fablet, D. Lucor, B. Iooss, J. Brajard, et al., Machine learning with data assimilation and uncertainty quantification for dynamical systems: a review, IEEE/CAA Journal of Automatica Sinica 10 (6) (2023) 1361–1387.

[18] R. Arcucci, J. Zhu, S. Hu, Y.-K. Guo, Deep data assimilation: integrating deep learning with data assimilation, Applied Sciences 11 (3) (2021) 1114.

[19] S. Cheng, C. Liu, Y. Guo, R. Arcucci, Efficient deep data assimilation with sparse observations and time-varying sensors, Journal of Computational Physics 496 (2024) 112581.

[20] T. H. Dur, R. Arcucci, L. Mottet, M. M. Solana, C. Pain, Y.-K. Guo, Weak constraint gaussian processes for optimal sensor placement, Journal of Computational Science 42 (2020) 101110.

[21] C. Buizza, C. Q. Casas, P. Nadler, J. Mack, S. Marrone, Z. Titus, C. Le Cornec, E. Heylen, T. Dur, L. B. Ruiz, et al., Data learning: Integrating data assimilation and machine learning, Journal of Computational Science 58 (2022) 101525.

[22] N. B. Erichson, L. Mathelin, Z. Yao, S. L. Brunton, M. W. Mahoney, J. N. Kutz, Shallow neural networks for fluid flow reconstruction with limited sensors, Proceedings of the Royal Society A 476 (2238) (2020) 20200097.

[23] T. Bolton, L. Zanna, Applications of deep learning to ocean data inference and subgrid parameterization, Journal of Advances in Modeling Earth Systems 11 (1) (2019) 376–399.

[24] J. Yu, J. S. Hesthaven, Flowfield reconstruction method using artificial neural network, Aiaa Journal 57 (2) (2019) 482–498.

[25] J. Wu, D. Xiao, M. Luo, Deep-learning assisted reduced order model for high-dimensional flow prediction from sparse data, Physics of Fluids 35 (10) (2023).

[26] F. Concas, J. Mineraud, E. Lagerspetz, S. Varjonen, X. Liu, K. Puolamäki, P. Nurmi, S. Tarkoma, Low-cost outdoor air quality monitoring and sensor calibration: A survey and critical analysis, ACM Transactions on Sensor Networks (TOSN) 17 (2) (2021) 1–44.

[27] S. Cheng, J.-P. Argaud, B. Iooss, D. Lucor, A. Ponçot, Error covariance tuning in variational data assimilation: application to an operating hydrological model, Stochastic Environmental Research and Risk Assessment 35 (5) (2021) 1019–1038.

[28] Z. Wu, S. Pan, F. Chen, G. Long, C. Zhang, S. Y. Philip, A comprehensive survey on graph neural networks, IEEE transactions on neural networks and learning systems 32 (1) (2020) 4–24.

[29] I. C. L. Environmental Research Group, London air quality network, `https://www.londonair.org.uk/LondonAir/Default.aspx` (2022 (accessed Nov 8, 2022)).

[30] K. Fukami, R. Maulik, N. Ramachandra, K. Fukagata, K. Taira, Global field reconstruction from sparse sensors with voronoi tessellation-assisted deep learning, Nature Machine Intelligence 3 (11) (2021) 945–951.

[31] D. Linsley, J. Kim, V. Veerabadran, C. Windolf, T. Serre, Learning long-range spatial dependencies with horizontal gated recurrent units, Advances in neural information processing systems 31 (2018).

[32] S. Jain, A. A. Presto, N. Zimmerman, Spatial modeling of daily pm2. 5, no2, and co concentrations measured by a low-cost sensor network: comparison of linear, machine learning, and hybrid land use models, Environmental Science & Technology 55 (13) (2021) 8631–8641.

[33] A. Dosovitskiy, L. Beyer, A. Kolesnikov, D. Weissenborn, X. Zhai, T. Unterthiner, M. Dehghani, M. Minderer, G. Heigold, S. Gelly, et al., An image is worth 16x16 words: Transformers for image recognition at scale, arXiv preprint arXiv:2010.11929 (2020).

[34] R. Fu, D. Xiao, I. M. Navon, F. Fang, L. Yang, C. Wang, S. Cheng, A non-linear non-intrusive reduced order model of fluid flow by auto-encoder and self-attention deep learning methods, International Journal for Numerical Methods in Engineering 124 (13) (2023) 3087–3111.

[35] X. Pan, D. Xiao, Domain decomposition for physics-data combined neural network based parametric reduced order modelling, Journal of Computational Physics 519 (2024) 113452.

[36] K. He, X. Chen, S. Xie, Y. Li, P. Dollár, R. Girshick, Masked autoencoders are scalable vision learners, arXiv preprint arXiv:2111.06377 (2021).

[37] Z. Wei, Jing; Li, Chinahighpm2.5, `https://zenodo.org/record/5919482#.Y2ty-NJByV4` (2022 (accessed Nov 8, 2022)).

[38] S. Müller, Geostat framework, `https://geostat-framework.org/` (2022 (accessed Nov 8, 2022)).

[39] W. Chen, Y. Li, B. J. Reich, Y. Sun, Deepkriging: Spatially dependent deep neural networks for spatial prediction, arXiv preprint arXiv:2007.11972 (2020).

[40] D. Ginsbourger, D. Dupuy, A. Badea, L. Carraro, O. Roustant, A note on the choice and the estimation of kriging models for the analysis of deterministic computer experiments, Applied Stochastic Models in Business and Industry 25 (2) (2009) 115–131.

[41] S. Cheng, I. C. Prentice, Y. Huang, Y. Jin, Y.-K. Guo, R. Arcucci, Data-driven surrogate model with latent data assimilation: Application to wildfire forecasting, Journal of Computational Physics (2022) 111302.

[42] S. Cheng, J. Chen, C. Anastasiou, P. Angeli, O. K. Matar, Y.-K. Guo, C. C. Pain, R. Arcucci, Generalised latent assimilation in heterogeneous reduced spaces with machine learning surrogate models, Journal of Scientific Computing 94 (1) (2023) 1–37.

[43] C. N. E. M. Centre, Chinese air quality, `https://air.cnemc.cn/` (2022 (accessed Nov 8, 2022)).

[44] Y. Zhan, Y. Luo, X. Deng, K. Zhang, M. Zhang, M. L. Grieneisen, B. Di, Satellite-based estimates of daily no2 exposure in china using hybrid random forest and spatiotemporal kriging model, Environmental science & technology 52 (7) (2018) 4180–4189.

[45] A. Hore, D. Ziou, Image quality metrics: Psnr vs. ssim, in: 2010 20th international conference on pattern recognition, IEEE, 2010, pp. 2366–2369.

[46] D. Lee, H. Park, I. K. Park, K. M. Lee, Joint blind motion deblurring and depth estimation of light field, in: Proceedings of the European Conference on Computer Vision (ECCV), 2018, pp. 288–303.